AIAA JOURNAL
Vol. 47, No. 8, August 2009

Computational and Experimental Investigation of a Nonslender Delta Wing

Raymond E. Gordnier* and Miguel R. Visbal†
U.S. Air Force Research Laboratory, Wright–Patterson Air Force Base, Ohio 45433-7512
and
Ismet Gursul‡ and Zhijin Wang§
University of Bath, Bath, England BA2 7AY, United Kingdom

DOI: 10.2514/1.37848

Computational simulations have been performed for a 50-deg-sweep delta wing with a sharp leading edge at a 15 deg angle of attack and moderate Reynolds numbers of $Re = 2 \times 10^5$, $Re = 6.2 \times 10^5$, and $Re = 2 \times 10^6$. A sixth-order compact-difference scheme with an eighth-order low-pass filter is used to solve the Navier–Stokes equations. Turbulence modeling has been accomplished using an implicit large eddy simulation method that exploits the high-order accuracy of the compact-difference scheme and uses the discriminating higher-order filter to regularize the solution. Computations have been performed on a baseline mesh of 11.3×10^6 grid points and a refined mesh of 35×10^6 grid points. An assessment of grid resolution showed that significantly finer-scale features of the flow could be captured on the refined mesh, providing a more accurate representation of the complex, unsteady, separated flow. Comparisons are also made with high-resolution particle image velocimetry images obtained for the two lower Reynolds numbers. The numerical results are examined to provide a description of the mean and instantaneous flow structure over the delta wing, including the separated vortical flow, vortex breakdown, surface flow features, and surface boundary-layer transition near the symmetry plane. The effect of Reynolds number on each of these features is assessed.

I. Introduction

LOW-SWEEP deltalike wings are a common feature in the design of current and proposed unmanned combat air vehicles (UCAVs) and small air vehicles. The complex flows over these types of maneuvering, unmanned aircraft may involve massive separation, which places numerous demands on a computational method. The flowfields are inherently unsteady and three dimensional. A combination of laminar, transitional, and turbulent flow regions may be present both on the surface of the wing and in the separated vortical flow. The ability to accurately simulate these types of flows and the complicated interactions between the separated vortical flow and the surface boundary layer is vital to capturing key performance coefficients (e.g., pitching moment coefficient, rolling moment coefficient). Therefore, a high degree of fidelity is required to satisfactorily compute these challenging unsteady flowfields.

Recently, Morton et al. [1], Morton [2], and Görtz [3] investigated the detached eddy simulation (DES) approach for improved prediction of the unsteady, vortical flowfields over delta wings. DES employs a traditional Reynolds-averaged Navier–Stokes turbulence model (Spallart–Allmaras) to represent the assumed turbulent wall boundary layer. The model then smoothly switches to a large eddy simulation (LES)-like model (Smagorinsky) in the separated region to more accurately represent the separated flow. The DES approach has been implemented into standard second-order-accurate flow codes [1,3]. In this paper, an alternative implicit large eddy simulation (ILES) approach is employed, which is based on a sixth-order-accurate computational scheme coupled with higher-order, low-pass filtering. This scheme is more appropriate for moderate Reynolds numbers at which laminar/transitional flows are encountered.

The computational approach employed in the present work solves the unsteady, three-dimensional Navier–Stokes equations using a well-validated and robust high-order solver [4–6]. All spatial derivatives are computed through high-order compact or Pade-type [7] difference methods. Schemes ranging from standard second-order to highly accurate sixth-order methods are possible. To enforce numerical stability, which can be compromised by mesh stretching, boundary conditions, and nonlinear phenomena, a higher-order, low-pass filter is used. This discriminating low-pass filter (up to 10th order) preserves the overall high-order accuracy of the spatial discretization while retaining stability for nonlinear applications. All these features have been implemented within the framework of an overset grid technology [8,9] that employs high-order interpolation methods to maintain the accuracy of the numerical scheme.

This higher-order computational approach also provides a unique opportunity to address the prediction challenges associated with massively separated turbulent flowfields. A new ILES modeling technique [10] has been developed based on the Pade differentiation and low-pass spatial filtering procedures. Rather than incorporating a subgrid scale model, this new scheme uses the discriminating filter to dissipate energy at the represented, but poorly resolved, high wave numbers. An attractive feature of this filtering ILES approach is that the governing equations and numerical procedure remain the same in all regions of the flow. In addition, the ILES method requires approximately half the computational resources of a standard dynamic Smagorinsky subgrid scale LES model. This results in a scheme capable of capturing with high-order accuracy the resolved part of the turbulent scales in an extremely efficient and flexible manner.

In recent years, a concerted effort has been made both experimentally [11–14] and computationally [15] to understand the distinctive characteristics of low-sweep delta wing flows. These investigations have primarily been performed at low Reynolds

Presented as Paper 894 at the 45th AIAA Aerospace Sciences Meeting and Exhibit, Reno, NV, 8–11 January 2007; received 2 April 2008; revision received 20 March 2009; accepted for publication 23 March 2009.

*Senior Research Aerospace Engineer, Computational Sciences Branch, Air Vehicles Directorate. Associate Fellow AIAA.
†Technical Area Leader, Computational Sciences Branch, Air Vehicles Directorate. Associate Fellow AIAA.
‡Professor of Aerospace Engineering, Department of Mechanical Engineering. Associate Fellow AIAA.
§Research Councils U.K. Academic Fellow, Department of Mechanical Engineering.

numbers ($<40,000$). Reviews by Gursul [16] and Gursul et al. [17] provide good summaries of this body of work. Interest in higher Reynolds numbers exists due to the operation of UCAVs and small air vehicles in moderate Reynolds number ranges ($1 \times 10^5 < Re < 1 \times 10^6$). In a previous work by two of the present authors, Gordnier and Visbal [18], the ILES method showed promise for simulating moderate Reynolds number flow over a low-sweep delta wing. In this paper, computations are performed for a 50-deg-sweep delta wing at Reynolds numbers of $Re = 2 \times 10^5$, 6.2×10^5, and 2×10^6. Experimental measurements have also been made at the two lower Reynolds numbers and are compared with the computed flowfield. A detailed description of the computed flow structure is then provided, including the effects of increasing Reynolds number.

II. Governing Equations

To properly model the complex unsteady viscous flows over delta wing configurations at moderate-to-high Reynolds numbers, the full compressible Navier–Stokes equations are selected. These equations are cast in strong conservative form, introducing a general time-dependent curvilinear coordinate transformation: $(x, y, z, t) \rightarrow (\xi, \eta, \zeta, \tau)$. In vector notation, and employing nondimensional variables, the equations are

$$\frac{\partial}{\partial \tau}\left(\frac{\mathbf{U}}{J}\right) + \frac{\partial \hat{F}}{\partial \xi} + \frac{\partial \hat{G}}{\partial \eta} + \frac{\partial \hat{H}}{\partial \zeta} = \frac{1}{Re}\left[\frac{\partial \hat{F}_v}{\partial \xi} + \frac{\partial \hat{G}_v}{\partial \eta} + \frac{\partial \hat{H}_v}{\partial \zeta}\right] \quad (1)$$

where $\mathbf{U} = \{\rho, \rho u, \rho v, \rho w, \rho E\}$ denotes the solution vector, and J is the transformation Jacobian. The inviscid and viscous fluxes, $\hat{F}$, $\hat{G}$, $\hat{H}$, $\hat{F}_v$, $\hat{G}_v$, and $\hat{H}_v$, can be found, for instance, in [19]. In these expressions, u, v, and w are the Cartesian velocity components, ρ the density, p the pressure, and T the temperature. All flow variables have been normalized by their respective freestream values (denoted throughout by the subscript ∞) except for pressure, which has been nondimensionalized by $\rho_\infty u_\infty^2$. The system of equations is closed using the perfect gas law $p = \rho T/\gamma M_\infty^2$, Sutherland's formula for viscosity, and the assumption of a constant Prandtl number, $Pr = 0.72$.

III. Numerical Methodology

A. Spatial Discretization

A finite difference approach is employed to discretize the flow equations. For any scalar quantity, ϕ, such as a metric, flux component, or flow variable, the spatial derivative ϕ' along a coordinate line in the transformed plane is obtained by solving the tridiagonal system:

$$\alpha\phi'_{i-1} + \phi'_i + \alpha\phi'_{i+1} = b\frac{\phi_{i+2} - \phi_{i-2}}{4\Delta\xi} + a\frac{\phi_{i+1} - \phi_{i-1}}{2\Delta\xi} \quad (2)$$

where $\alpha = \frac{1}{3}$, $a = \frac{14}{9}$, and $b = \frac{1}{9}$. This choice of coefficients yields at interior points the compact five-point, sixth-order algorithm of Lele [20]. At boundary points $1, 2, IL-1$, and IL, fourth- and fifth-order one-sided formulas are used that retain the tridiagonal form of the interior scheme [4,7].

Compact-difference discretizations, like other centered schemes, are nondissipative and are therefore susceptible to numerical instabilities due to the growth of spurious high-frequency modes. These difficulties originate from several sources, including mesh nonuniformity, approximate boundary conditions, and nonlinear flow features. To ensure long-term numerical stability while retaining the improved accuracy of the spatial compact discretization, a high-order implicit filtering technique [6,21] is incorporated. If a component of the solution vector is denoted by ϕ, filtered values $\hat{\phi}$ are obtained by solving the tridiagonal system,

$$\alpha_f\hat{\phi}_{i-1} + \hat{\phi}_i + \alpha_f\hat{\phi}_{i+1} = \Sigma_{n=0}^{N}\frac{a_n}{2}(\phi_{i+n} + \phi_{i-n}) \quad (3)$$

Equation (3) is based on templates proposed in [20,22] and, with the proper choice of coefficients, provides a $2N$th-order formula on a $2N+1$ point stencil. The coefficients, $a_0, a_1, \ldots, a_N$, derived in terms of the single parameter α_f using Taylor- and Fourier-series analysis, are given in [4], along with detailed spectral filter responses. In the present study, an eighth-order filter operator with $\alpha_f = 0.3$ is applied at interior points. For near-boundary points, the filtering strategies described in [5,6] are employed. Filtering is applied to the conserved variables and sequentially in each coordinate direction.

B. Time Integration

For wall-bounded viscous flows, the stability constraint of explicit time-marching schemes is too restrictive and the use of an implicit approach becomes necessary. For this purpose, the implicit approximately factored scheme of Beam and Warming [23] is incorporated and augmented through the use of Newton-like subiterations to achieve second-order temporal and sixth-order spatial accuracy. In delta form, the scheme may be written as

$$\begin{aligned}
&\left[J^{-1^{p+1}} + \phi^i\Delta\tau\delta_\xi^{(2)}\left(\frac{\partial \hat{F}^p}{\partial U} - \frac{1}{Re}\frac{\partial \hat{F}_v^p}{\partial U}\right)\right]J^{p+1} \\
&\times\left[J^{-1^{p+1}} + \phi^i\Delta\tau\delta_\eta^{(2)}\left(\frac{\partial \hat{G}^p}{\partial U} - \frac{1}{Re}\frac{\partial \hat{G}_v^p}{\partial U}\right)\right]J^{p+1} \\
&\times\left[J^{-1^{p+1}} + \phi^i\Delta\tau\delta_\zeta^{(2)}\left(\frac{\partial \hat{H}^p}{\partial U} - \frac{1}{Re}\frac{\partial \hat{H}_v^p}{\partial U}\right)\right]\Delta U \\
&= -\phi^i\Delta\tau\Bigg[J^{-1^{p+1}}\frac{(1+\phi)U^p - (1+2\phi)U^n + \phi U^{n-1}}{\Delta\tau} \\
&+ U^p(1/J)_\tau^p + \delta_\xi\left(\hat{F}^p - \frac{1}{Re}\hat{F}_v^p\right) + \delta_\eta\left(\hat{G}^p - \frac{1}{Re}\hat{G}_v^p\right) \\
&+ \delta_\zeta\left(\hat{H}^p - \frac{1}{Re}\hat{H}_v^p\right)\Bigg]
\end{aligned} \quad (4)$$

where

$$\phi^i = \frac{1}{1+\phi}, \qquad \Delta U = U^{p+1} - U^p \quad (5)$$

For the first subiteration, $p = 1$, $U^p = U^n$, and, as $p \rightarrow \infty$, $U^p \rightarrow U^{n+1}$. The spatial derivatives in the implicit (left-hand-side) operators are represented using standard second-order centered approximations, whereas high-order discretizations are employed for the explicit terms (right-hand side). Although not shown in Eq. (4), nonlinear artificial dissipation terms [24,25] are appended to the implicit operator to enhance stability. In addition, for improved efficiency, the approximately factored scheme is recast in diagonalized form [26]. Any degradation in solution accuracy caused by the second-order implicit operators, artificial dissipation, and the diagonal form are eliminated through the use of subiterations. Typically, three subiterations per time step are adequate to reduce the error below the temporal truncation error given the small time steps required due to physical considerations.

C. Boundary Conditions

The boundary conditions for the flow domain are prescribed as follows. At the solid surface, the no-slip condition is applied (i.e., $u = v = w = 0$). In addition, the wall is assumed to be isothermal ($T_w = T_{adb}$), and the normal pressure gradient condition $\frac{\partial p}{\partial n} = 0$ is specified. Symmetry conditions ($v = 0$, $\frac{\partial}{\partial y}(u, w, p, \rho) = 0$) are employed on the symmetry plane of the delta wing, $\eta = 0$. On the inflow and lower boundaries, uniform flow is specified, whereas at the outflow, upper, and side boundaries, all variables are extrapolated from the interior using a first-order extrapolation.

The treatment of the far-field boundaries is based on the approach proposed and evaluated previously in [27] for some acoustic benchmark problems. This method exploits the properties of the high-order, low-pass filter in conjunction with a rapidly stretched mesh. As grid spacing increases away from the region of interest, energy not supported by the stretched mesh is reflected in the form of

high-frequency modes that are annihilated by the discriminating spatial filter operator. An effective "buffer" zone is therefore created using a few grid points in each coordinate direction to rapidly stretch to the far-field boundary. No further need for the explicit incorporation of complicated boundary conditions or modifications to the governing equations is then required.

D. Implicit Large Eddy Simulation Methodology

The ILES method to be used in the present computations was first proposed and investigated by Visbal et al. [10]. The underlying idea behind the approach is to capture with high accuracy the resolved part of the turbulent scales while providing for a smooth regularization procedure to dissipate energy at the represented, but poorly resolved, high wave numbers of the mesh. In the present computational procedure, the sixth-order compact-difference scheme provides the high accuracy whereas the low-pass spatial filters provide the regularization of the unresolved scales. All this is accomplished with no additional subgrid scale models as in traditional LES approaches. Although this method bears similarities with monotone implicit LES approaches, it differs from them in two main respects. First, sixth-order-accurate compact schemes are used for the discretization of the spatial derivatives. Secondly, dissipation at high wave numbers is not provided implicitly by the inherent dissipation of the numerical scheme but rather through the high-order spatial filter, which is applied explicitly to the evolving solution.

IV. Experimental Setup

Particle image velocimetry (PIV) measurements were carried out in the 2.13×1.52 m working cross section of a closed circuit wind tunnel at the University of Bath, England. The tunnel has two viewing windows made from optical glass, one at the sidewall and one at the bottom floor, to facilitate visualization and laser illumination. Experiments were conducted using an aluminum, low-sweep delta wing ($\Lambda = 50$ deg). The model, mounted on the high-incidence rig, had a chord length of $c = 310$ mm and a thickness of $t = 5$ mm, giving a thickness-to-chord ratio of $t/c = 1.6\%$. The model had 45 deg beveled sharp leading edges and a square trailing edge. The wing surface was painted black to minimize reflections.

Experiments were conducted at a wing incidence of $\alpha = 15$ deg. A total of three Reynolds numbers ($Re = U_\infty c/\nu$, where U_∞ is the freestream velocity and ν is the fluid kinematic viscosity) were tested: $Re = 2 \times 10^5$, 4×10^5, and 6.2×10^5. The flow was seeded with smoke generated by a Jem ZR12-AL smoke generator, with a mean diameter of 1 μ. To identify the leading-edge vortex core locations for each Re, crossflow PIV measurements were carried out at 20% chord from the wing apex. Illumination was provided from a pair of pulsed mini Nd:YAG lasers with a maximum energy of 120 mJ per pulse by laser sheets generated by a combination of cylindrical and spherical lenses. The laser sheet was set perpendicular to the freestream and cutting through the wing surface at 20% chord. The PIV camera was put into an optical glass box to protect the camera from contamination by the seeding particles. The camera was then placed inside the wind tunnel downstream of the delta wing, thus measuring the crossflow velocity field. Vortex core locations were identified from these crossflow PIV results. The laser sheet was then aligned with the vortex core so that the velocity field in a plane through the vortex core was measured. The measurement plane covered a distance of 55% chord.

The digital particle images from the PIV measurement were taken using an 8-bit charge-coupled device camera with a resolution of 4.2×10^6 pixels. The commercial software package Insight v6.0 and a Hart cross-correlation algorithm were used to analyze the images. In the image processing, an interrogation window size of 32×32 pixels was used to produce the velocity vectors. The effective grid size was varied from 1.5 mm in crossflow planes to 1.8 mm in a plane through the vortex cores. Sequences of 800 and 3000 instantaneous frames, corresponding to the crossflow and vortex core plane measurements, respectively, were taken at a frame rate of 3.75 Hz. The time-averaged velocity and vorticity fields were calculated.

V. Delta Wing Computations

Figure 1 shows the equivalent delta wing geometry used in the computations. Two different grids were developed for the present computations, assuming flow symmetry to reduce computational requirements. The assumption of symmetry is reasonable for these lower-sweep delta wings for which the proximity of the leading-edge vortices to each other is reduced due to the lower sweep angle. The coarser H–O mesh consists of 268 points in the axial direction (171 located on the wing), 231 points in the circumferential direction, and 183 points normal to the wing. A typical cross section of the grid and the surface mesh are shown in Figs. 2a and 2b, respectively. The nominal spacing on the wing (x, y, and z normalized by the root chord c) is $\Delta x = 0.0059$ in the axial direction and $\Delta z = 0.00001$ in the normal direction at the surface. In the core of the vortex at the trailing edge of the wing, the grid spacing is $\Delta y_{\text{core}} = 0.0069$ and $\Delta z_{\text{core}} = 0.002$. A refined mesh of $442 \times 361 \times 219$ grid points was also developed. The objective of this mesh refinement was to significantly decrease the mesh spacing in the axial and spanwise directions in the core of the vortex. The axial spacing on the wing was halved to $\Delta x = 0.003$. At the trailing edge, the spanwise spacing in the vortex core is also halved to $\Delta y_{\text{core}} = 0.0035$. The spanwise spacing at the upper symmetry plane has also been reduced from $\Delta y = 0.03$ to 0.0149. To meet the temporal resolution requirements, a small nondimensional time step of $\Delta\tau = 6.25 \times 10^{-5}$ is specified. This provides a minimum of 500 time steps per cycle for the maximum anticipated frequencies.

The computations on these large meshes were accomplished using a domain decomposition approach for parallel processing by exploiting the high-order overset grid capabilities [9] available in the code. The fine mesh was decomposed into 172 grids with approximately equal numbers of grid points for each subgrid. A five-point overlap between grids is employed. Each subgrid was then assigned to its own individual processor.

Computations are performed for the same conditions as in the experiment, $\alpha = 15$ deg and $Re = 2 \times 10^5$ and 6.2×10^5. A somewhat higher Reynolds number, $Re = 2 \times 10^6$, is also computed for comparison purposes. A freestream Mach number, $M_\infty = 0.1$, and a freestream density, $\rho_\infty = 1.21$ kg/m^3, are specified. The effect of mesh resolution on the numerical results for $Re = 6.2 \times 10^5$ and comparisons with the experimental measurements for $Re = 2 \times 10^5$ and 6.2×10^5 are made to validate the computational results. A description of the mean vortical flow structure based on the fine mesh computations is then presented. The effect of Reynolds number on the flow structure is also investigated.

V. Grid Resolution Study

Figures 3a and 3b demonstrate the impact of mesh refinement on the global structure of the vortex for the mean and instantaneous flows, respectively. Isosurfaces of constant axial vorticity colored by density contours highlight the general vortex structure. The fine grid solution captures smaller-scale unsteady features of the vortical flow (Fig. 3b), both in the shear layer that separates from the leading edge

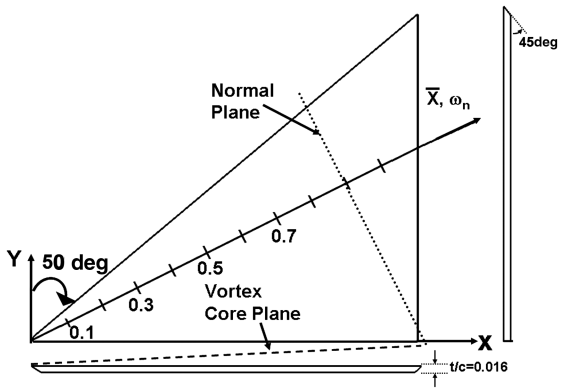

Fig. 1 Computational delta wing geometry.

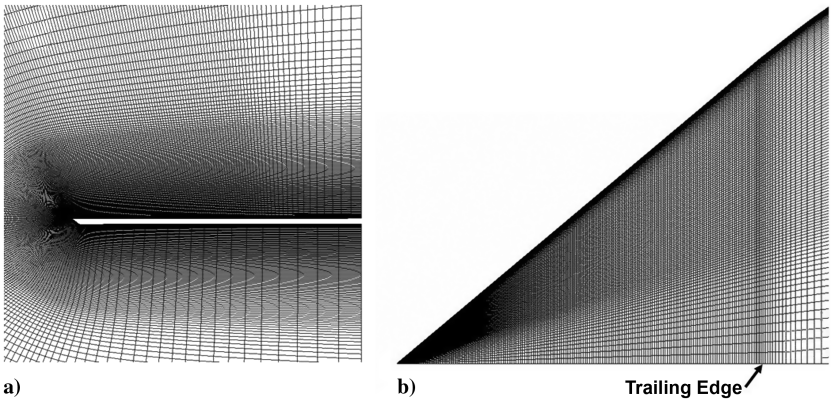

Fig. 2 Baseline delta wing grid structure: a) typical cross section, and b) surface grid.

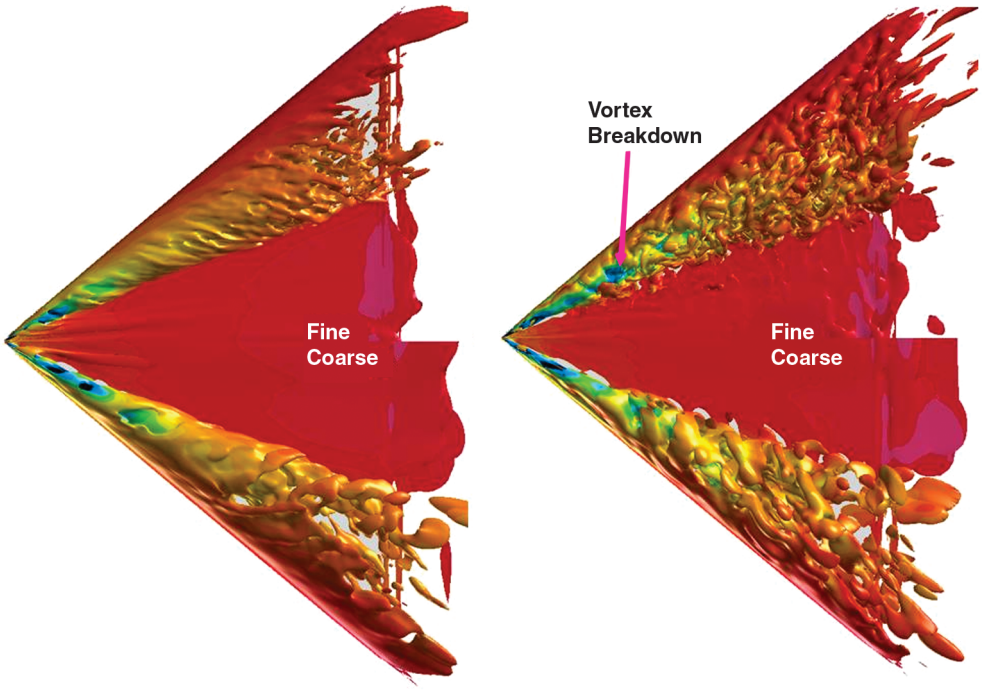

Fig. 3 Isosurfaces of constant axial vorticity colored by density contours, $\alpha = 15$ deg, $Re = 6.2 \times 10^5$: a) mean vortex structure, and b) instantaneous vortex structure.

and rolls up to form the vortex as well as in the core of the vortex downstream of breakdown. As a result, the mean flow exhibits more clear-cut, small-scale substructures in the outer shear layer and in the breakdown region downstream.

The effect of grid refinement on the computed flowfield can be further understood by examining the structure in planes normal to the vortex core, as shown in Fig. 1. Figures 4a and 4b compare the vortex structure upstream of breakdown at a location of $\bar{x} = 0.1429$. On each mesh, primary, secondary, and tertiary vortices are observed, as well as a second vortex of the same sign as the primary vortex outboard near the leading edge. This type of dual vortex system has been observed previously for low-sweep delta wings [12,14,15] and results from the interaction of the secondary flow with the primary shear layer. Increased unsteadiness resulting in significantly higher levels of turbulent kinetic energy is obtained with refinement, Fig. 4c. Enhancement of the boundary-layer eruptive behavior induced by the vortex surface interaction and the resulting wandering of the primary vortex core are responsible for this increase in the fluctuations. This type of unsteady behavior has been described in detail previously [15,28–30]. The net result is increased turbulent dissipation that weakens the primary and secondary vortices, Fig. 4a.

The weakening of the vortex upstream of breakdown with grid resolution is seen in Figs. 5a and 5b, in which contours of the axial velocity on a plane through the vortex core are plotted. Upstream of breakdown, the peak jet velocity in the vortex core is smaller on the fine grid, Fig. 5a. This, again, is a result of the higher fluctuations obtained upstream of breakdown with grid refinement, Figs. 5c and 5d. Although the strength of the upstream vortex has been diminished, this has not resulted in a noticeable change in the vortex breakdown location.

Downstream of breakdown, the fine-grid solution exhibits a much more detailed flow structure with significantly smaller scales being captured, Fig. 6. Both the mean and instantaneous flows on the fine grid show more small-scale features in the outer shear layer that rolls up to form the vortex, Figs. 6a and 6c, as well as in the vortex core itself. Enhanced interactions of these structures with the surface boundary layer are also seen as they move across the wing surface. The resulting turbulent kinetic energy levels are smaller on the fine mesh but the turbulent kinetic energy is more evenly distributed throughout the vortex core. This contrasts with the behavior observed upstream of breakdown.

In practical applications, the interest is often in surface values such as the pressure or pressure fluctuations (buffeting). Figures 7a and 7b

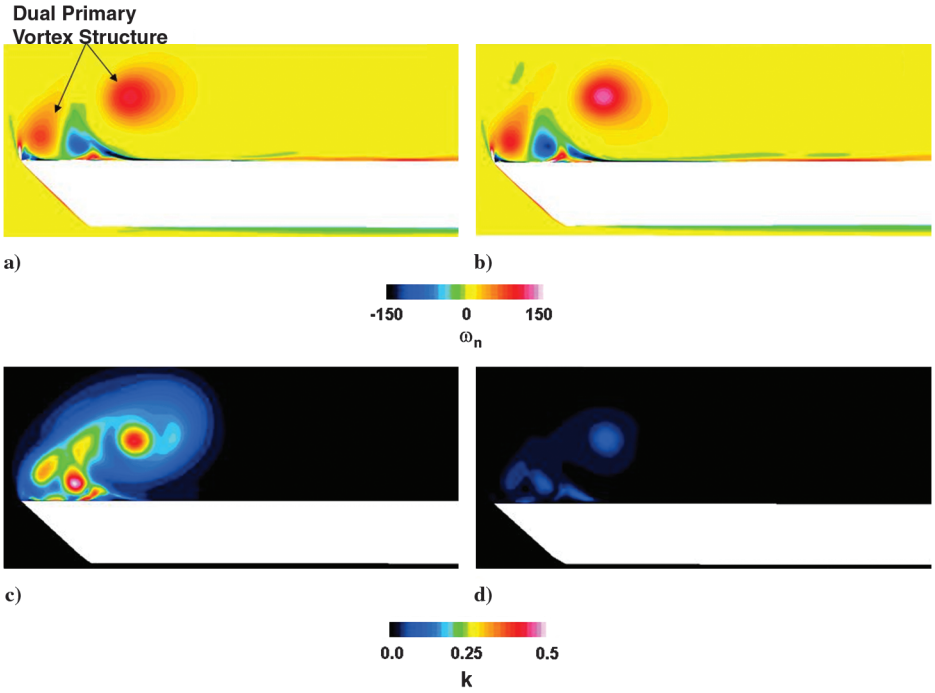

Fig. 4 Contours of the mean axial vorticity and turbulent kinetic energy in a crossflow plane normal to the vortex, $\alpha = 15$ deg, $Re = 6.2 \times 10^5$, $\bar{x} = 0.1429$: a, c) fine mesh; and b, d) coarse mesh.

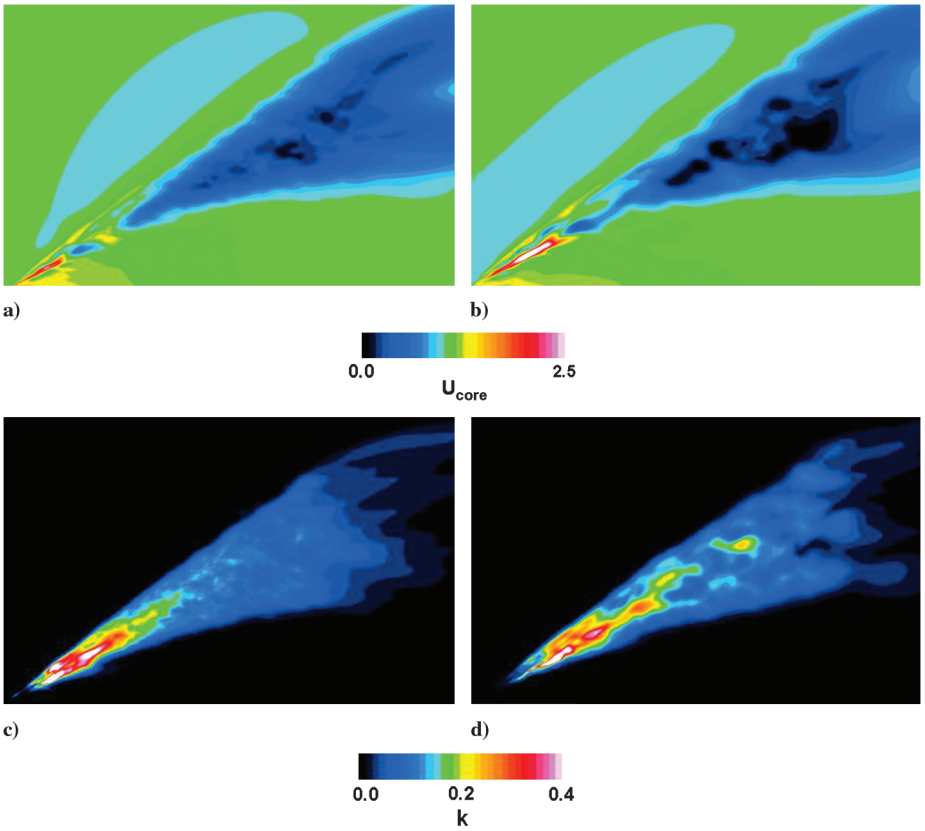

Fig. 5 Contours of the mean axial velocity and turbulent kinetic energy on a plane through the vortex core, $\alpha = 15$ deg, $Re = 6.2 \times 10^5$: a, c) fine mesh; and b, d) coarse mesh.

compare the mean surface pressure coefficient and the surface pressure fluctuations, respectively, on the two meshes. Because the vortex upstream of breakdown is weaker on the fine mesh, the corresponding peak suction levels under the vortex are reduced. On the fine grid, the surface pressure fluctuations are stronger upstream of breakdown and in the breakdown region. A narrow region of higher levels of fluctuation extends a shorter distance downstream with refinement.

The grid resolution study has shown that significantly more of the unsteady, fine-scale features of the flow are captured on the fine

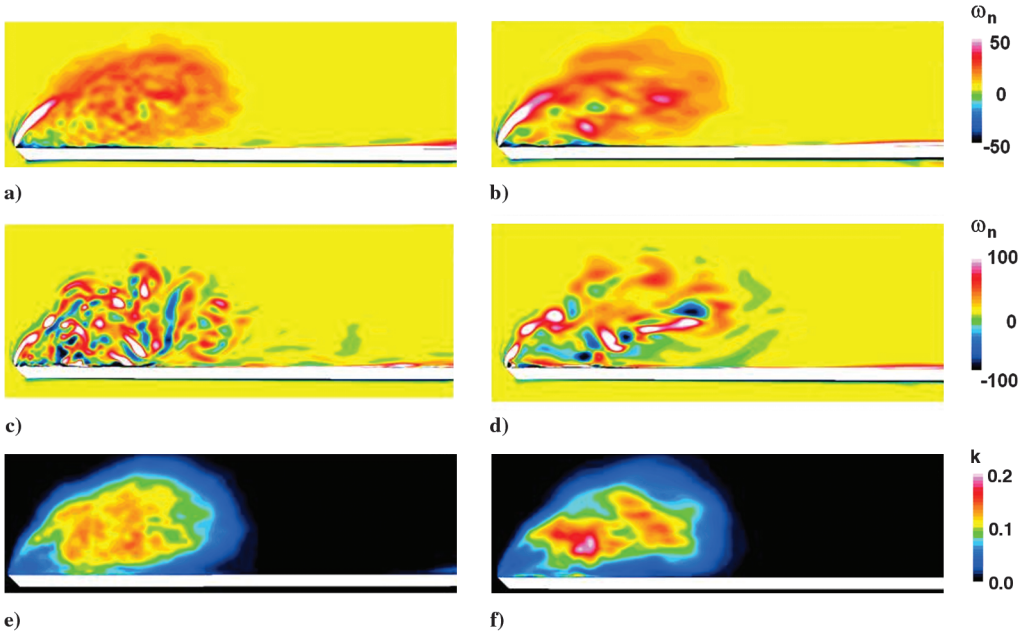

Fig. 6 Contours of the mean (a, b) and instantaneous (c, d) axial vorticity and turbulent kinetic energy (e, f) in a crossflow plane normal to the vortex, $\alpha = 15$ deg, $Re = 6.2 \times 10^5$, $\bar{x} = 0.85$: a, c, and e) fine mesh; and b, d, and f) coarse mesh.

mesh. These results demonstrate that sufficient grid resolution remains important for correctly modeling this type of transitional flow even with the higher-order computational method employed. All further discussions in this paper will only consider the solutions on the fine mesh.

B. Comparison with Experiment

Comparisons between the experimental PIV measurements and the computations are made for two Reynolds numbers, $Re = 2 \times 10^5$ and 6.2×10^5. This was accomplished by interpolating the computational results onto the PIV grid to provide an equivalent computational representation. The computed mean flow was obtained by averaging over a period of 12.5 characteristic times based on a convective time scale of c/U_∞. Figure 8 compares the mean vorticity and velocity magnitude at the axial location of $x = 0.2$ for $Re = 2 \times 10^5$. Good qualitative agreement is seen between the computation and the experiment, with all the salient features in the experiment being reproduced in the computation. The computation produces a somewhat stronger vortex at this location, Figs. 8a and 8c, with what appears to be a correspondingly enhanced secondary flow. The mean velocity magnitude on a plane through the vortex core, Fig. 9, also shows good agreement between the computation and the experiment, with vortex breakdown occurring at approximately the same axial location. The computation exhibits a sharper delineation of the vortex breakdown than the experimental measurements. A comparison of the instantaneous velocity magnitude on the same plane, Fig. 10, also displays a striking similarity between the computation and the experiment with the primary unsteady flow structures observed in the experiment reproduced in the computation.

Examination of the results in the crossflow plane at the higher Reynolds number, $Re = 6.2 \times 10^5$, also reveals good correlation between the PIV measurements and the computation, Fig. 11. The computed and experimental mean velocity magnitude agree particularly well, Figs. 11c and 11d, whereas a slightly smaller vorticity magnitude is noted in the core of the computed primary vortex. Both the experiment and the computation in Fig. 12 show a conically shaped region of low speed flow associated with vortex breakdown that penetrates approximately the same distance upstream with similar velocity levels. In between this region and the intact vortex core denoted by the high jetlike velocities lies a region over which the breakdown of the vortex occurs. This region is longer and has a more complex structure in the computation and will be discussed further in Secs. VI.A and VII.A. The initial breakdown of the vortex in the computations occurs slightly upstream of the experimental location.

The overall good agreement between the computation and the experiment provides confidence that the ILES approach is properly capturing the relevant flow features for this separated delta wing flow at moderate Reynolds numbers. Because the full three-dimensional flowfield is available from the computations, only these results will be described in detail in Secs. VI and VII.

VI. Computed Mean Flow Structure

The mean flow structure over the delta wing will now be described for the computations on the fine mesh. Three different Reynolds numbers, $Re = 2 \times 10^5$, 6.2×10^5, and 2×10^6, are investigated to assess the effect of increasing Reynolds number on the flow. The mean flow quantities are obtained by averaging over a period of 12.5 characteristic times.

A. Mean Vortex Breakdown Structure

The onset of vortex breakdown can be seen by examining the vortex structure on a vertical plane through the vortex core. Figure 13 displays contours of the mean axial velocity for each Reynolds number. A jetlike velocity region characterizes the intact vortex core upstream of breakdown. The peak axial velocity at $x/c = 0.14$ decreases with increasing Reynolds number, Table 1. Downstream, a transformation from this jetlike flow to a wakelike flow occurs. This switch from jetlike to wakelike flow is indicative of the onset of vortex breakdown (see, for instance, [31,32]). In none of the cases is actual flow reversal achieved in the wake region as observed for the vortex breakdown over higher-sweep delta wings. In Table 1, the location of the onset of vortex breakdown is given for each Reynolds number. As the Reynolds number is increased from 2×10^5 to 6.2×10^5, the breakdown location moves upstream. As the Reynolds number is raised further to 2×10^6, the breakdown location moves back downstream.

A progressive change in the character of the onset of vortex breakdown due to transitional flow effects is seen with increasing Reynolds number. For $Re = 2 \times 10^5$, a sharp switch from the jetlike to wakelike flow occurs, Figs. 13a. There is a distinct narrowing of the wake flow at a short distance downstream, followed by a gradual broadening of the wake region. As the Reynolds number is increased to $Re = 6.2 \times 10^5$, Fig. 13b, the wake region separates into two

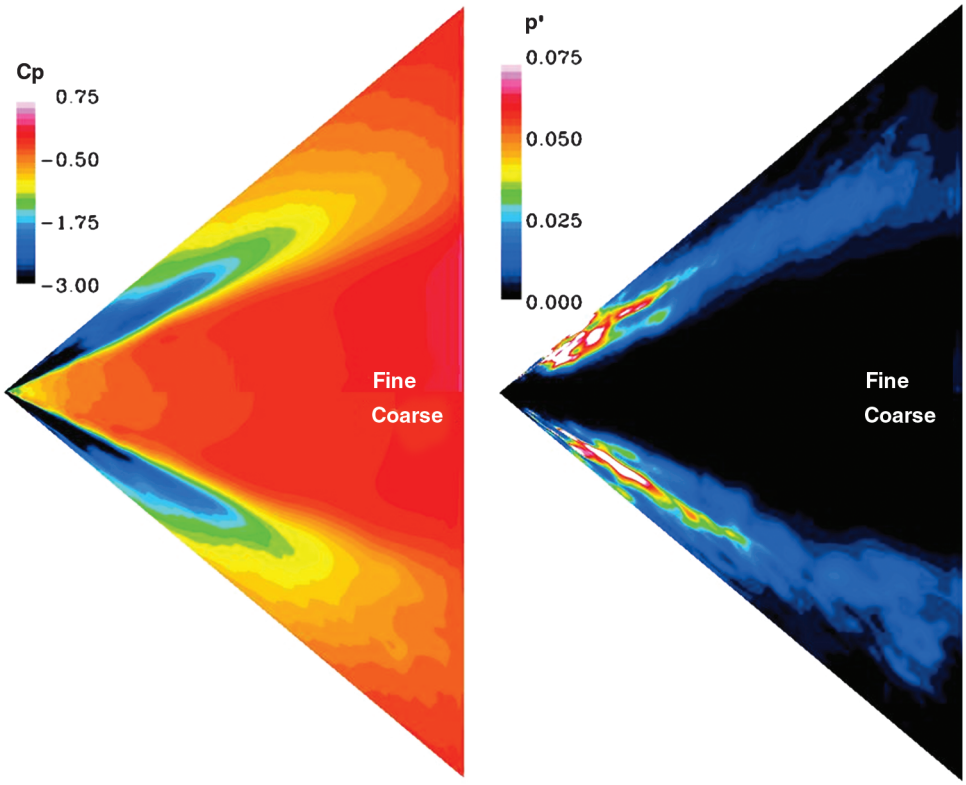

Fig. 7 Comparison of the coarse and fine meshes for $\alpha = 15$ deg, $Re = 6.2 \times 10^5$: a) mean surface pressure coefficient and b) surface pressure fluctuations.

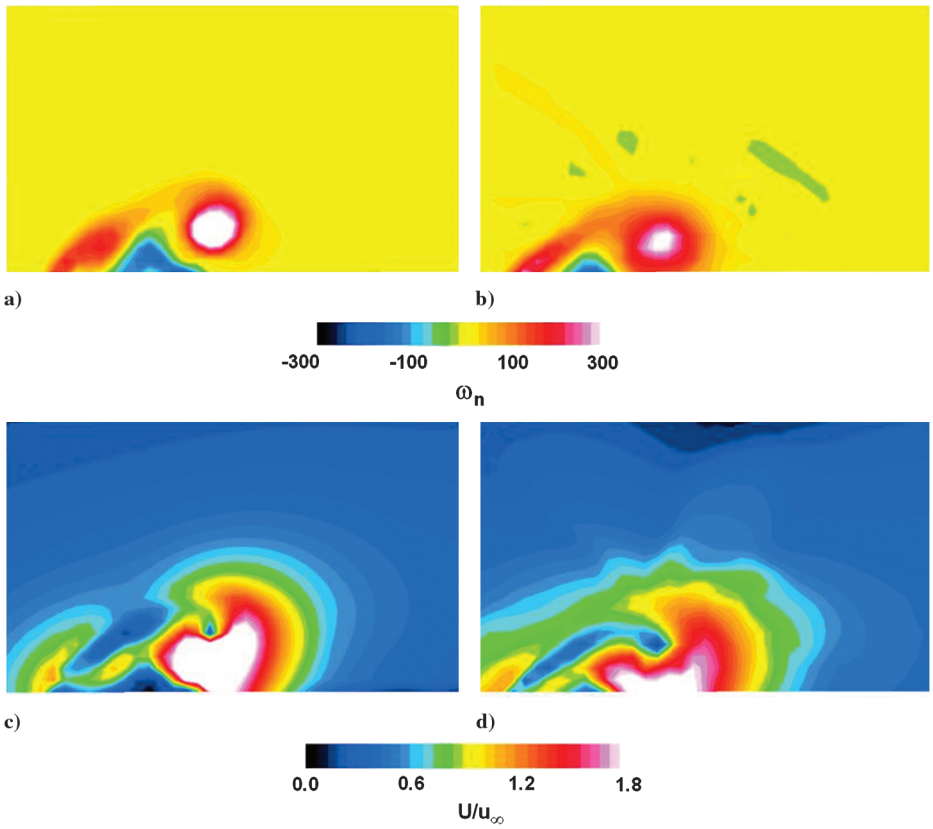

Fig. 8 Comparison of the computation (a, c) and PIV measurements (b, d) on the crossflow plane $x = 0.2$, $Re = 2 \times 10^5$: a, b) mean vorticity; and c, d) mean crossflow velocity magnitude.

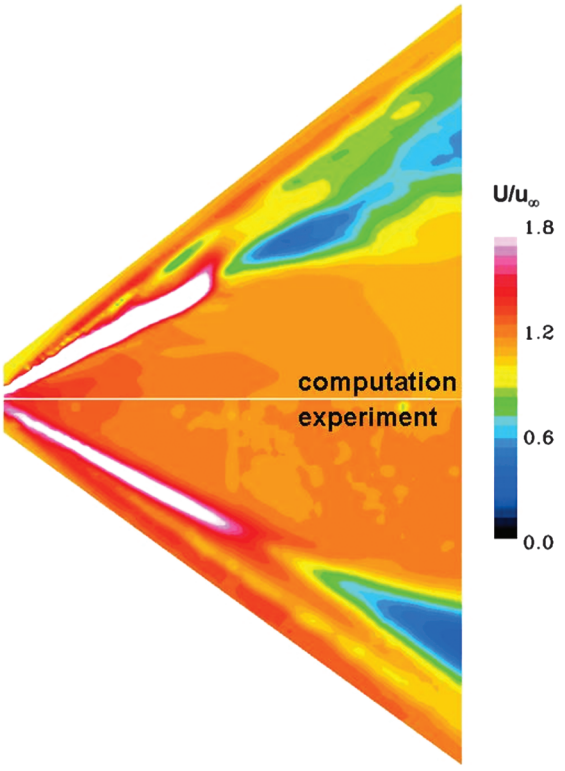

Fig. 9 Comparison of the experimental and computational mean velocity magnitude on a plane through the vortex core, $Re = 2 \times 10^5$.

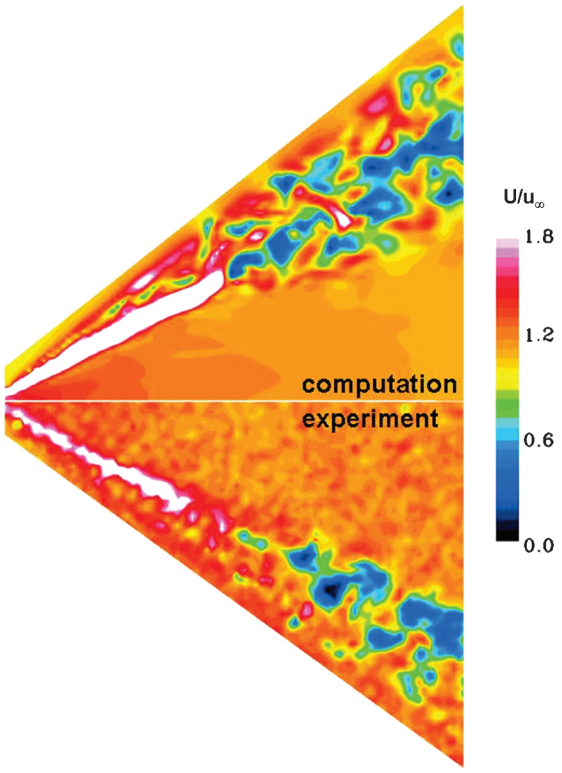

Fig. 10 Comparison of the experimental and computational instantaneous velocity magnitude on a plane through the vortex core, $Re = 2 \times 10^5$.

regions. The breakdown of the vortex thus appears to occur in two stages. In the first region, a change from the strong jetlike velocity in the core to a more diffuse region of lower velocities is seen for a limited longitudinal extent. In the downstream portion of this stage, there is a partial recovery of the velocity before the onset of a stronger conically shaped wake in the second stage. At the highest Reynolds number, this two-stage process is replaced by a single, less abrupt switch from jetlike to wakelike flow at the onset of breakdown, Fig. 13c. The wake flow has a conically shaped character similar to the second stage of the $Re = 6.2 \times 10^5$ case with a similar onset location.

Associated with the change from jetlike to wakelike flow is a switch in sign of the azimuthal vorticity [33]. Contour plots of the

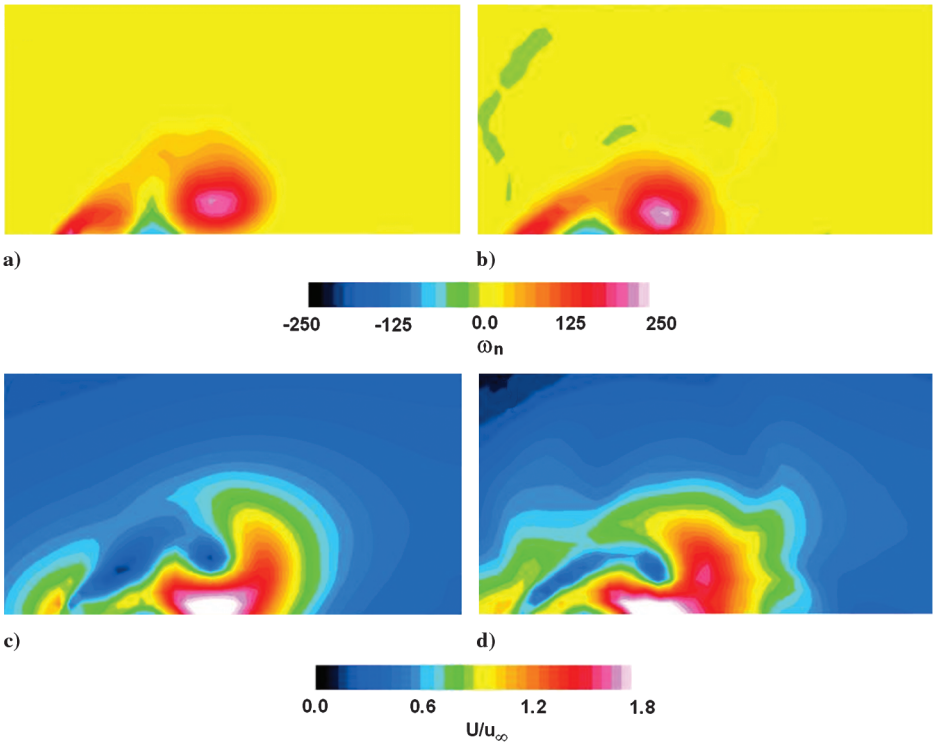

Fig. 11 Comparison of the computation (a, c) and PIV measurements (b, d) on the crossflow plane $x = 0.2$, $Re = 6.2 \times 10^5$: a, b) mean vorticity; and c, d) mean crossflow velocity magnitude.

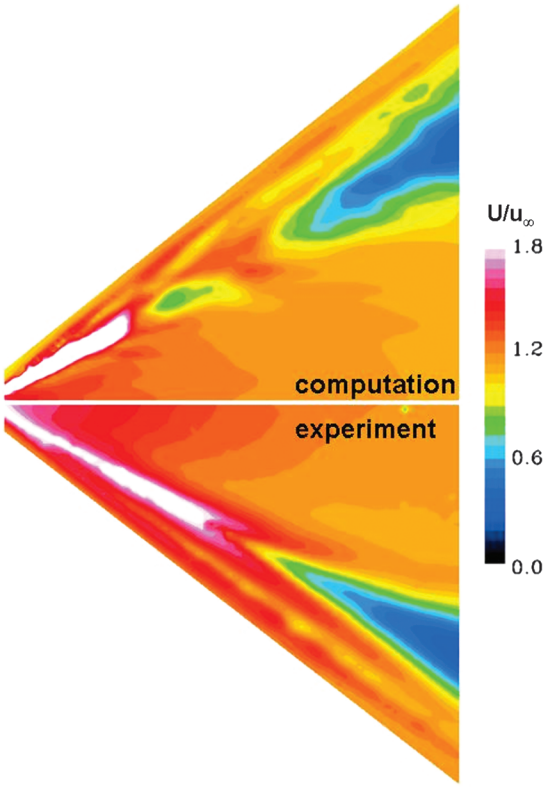

Fig. 12 Comparison of the experimental and computational mean velocity magnitude on a plane through the vortex core, $Re = 6.2 \times 10^5$.

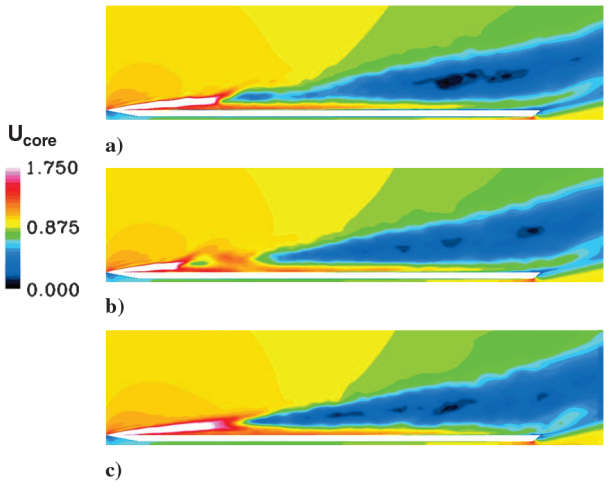

Fig. 13 Mean axial velocity contours on a vertical plane through the vortex core: a) $Re = 2 \times 10^5$, b) $Re = 6.2 \times 10^5$, and c) $Re = 2 \times 10^6$.

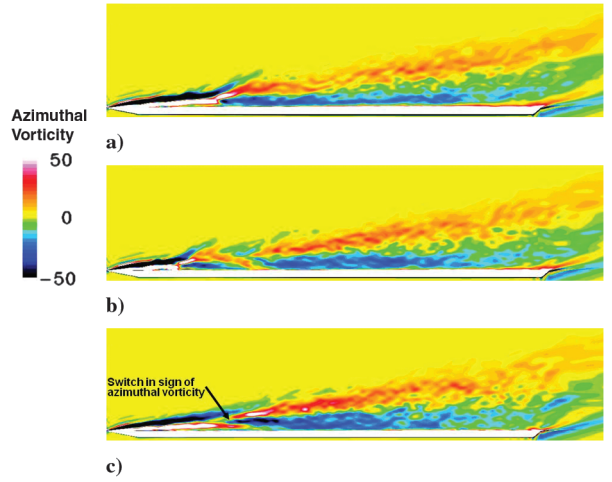

Fig. 14 Mean azimuthal vorticity contours on a vertical plane through the vortex core: a) $Re = 2 \times 10^5$, b) $Re = 6.2 \times 10^5$, and c) $Re = 2 \times 10^6$.

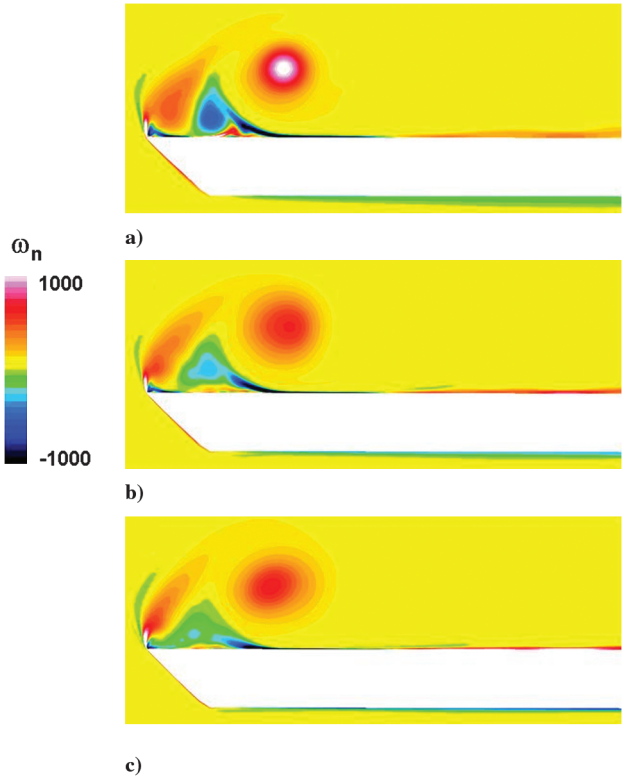

Fig. 15 Mean axial vorticity contours on a crossflow plane located at $\bar{x} = 0.175$: a) $Re = 2 \times 10^5$, b) $Re = 6.2 \times 10^5$, and c) $Re = 2 \times 10^6$.

mean azimuthal vorticity in the vortex core are given in Fig. 14. For $Re = 6.2 \times 10^5$, Fig. 14b, two distinct regions associated with the vortex breakdown are again observed. An initial switch in sign of the azimuthal vorticity is followed by a region in which a partial switch back to the original vorticity distribution occurs, albeit with lower vorticity levels. This region is terminated by a second switch in sign of the azimuthal vorticity. At the highest Reynolds number, Fig. 14c, the region downstream of the switch in sign of vorticity shows a much more regular, conical shape.

Table 1 Mean breakdown location, x/c_{bd}, and mean maximum core velocity, $\bar{u}_{\text{core}}$, at $x/c = 0.14$

Re	x/c_{bd}	$\bar{u}_{\text{core}}$
2×10^5	0.27	2.91
6.2×10^5	0.16	2.70
2×10^6	0.32	2.21

B. Mean Vortex Structure in Crossflow Planes Normal to the Vortex Core

The mean vortex structure may be further elucidated by analyzing the flow on crossflow planes normal to the vortex core (see Fig. 1) at locations both upstream and downstream of breakdown. Figure 15 plots the mean axial vorticity on a plane upstream of breakdown located at $\bar{x} = 0.175$. For all cases, distinct primary and secondary vortices are present. As the Reynolds number is increased, the primary vortex weakens and becomes more diffuse. Correspond-

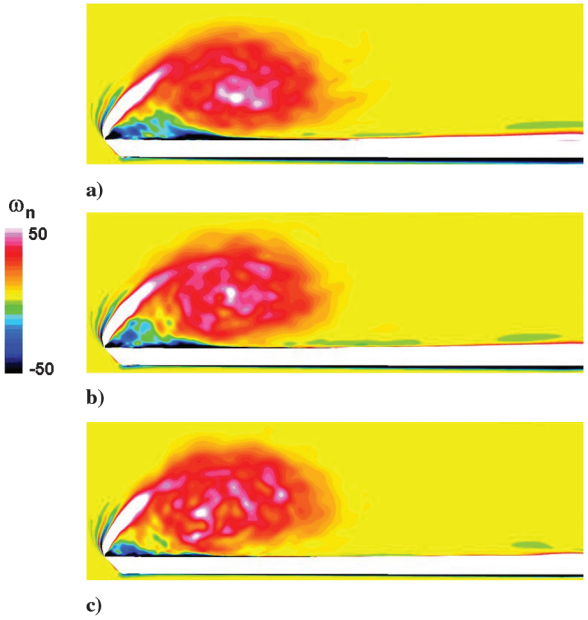

Fig. 16 Mean axial vorticity contours on a crossflow plane located at $\bar{x} = 0.612$: a) $Re = 2 \times 10^5$, b) $Re = 6.2 \times 10^5$, and c) $Re = 2 \times 10^6$.

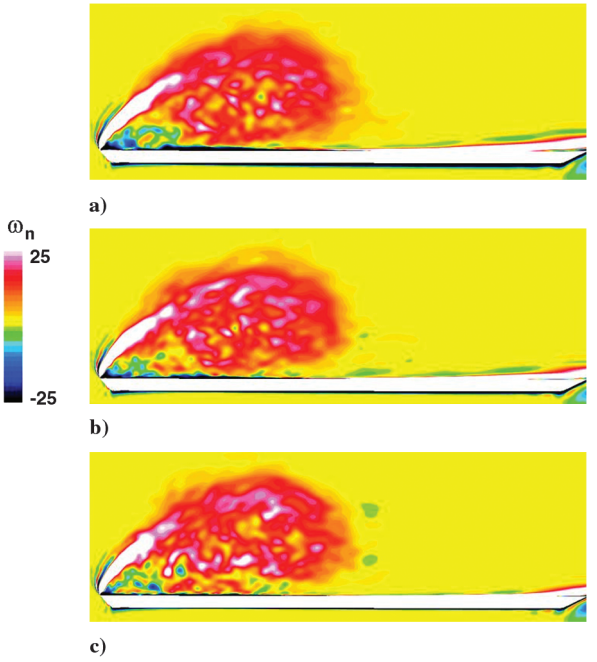

Fig. 17 Mean axial vorticity contours on a crossflow plane located at $\bar{x} = 0.875$: a) $Re = 2 \times 10^5$, b) $Re = 6.2 \times 10^5$, and c) $Re = 2 \times 10^6$.

ingly, there is a weakening of the secondary flow and the secondary separation point moves outboard toward the leading edge. At the lowest Reynolds number, Fig. 15a, a second, weaker vortical structure of the same sign as the primary vortex is seen outboard toward the leading edge. Similar dual vortex structures have been observed in previous computations [15] and experiments [12,14] and arise from the interaction of the secondary flow with the primary shear layer separating from the leading edge. As the secondary flow weakens with increasing Reynolds number, this interaction is reduced and the dual primary vortex structure is less pronounced.

Mean axial vorticity on a plane downstream of breakdown at a location near the midchord of the wing, $\bar{x} = 0.612$, is shown in Fig. 16. At this location, values of vorticity have been substantially reduced. The vortex has a more oval shape and is composed of a number of small-scale features. These small-scale structures become

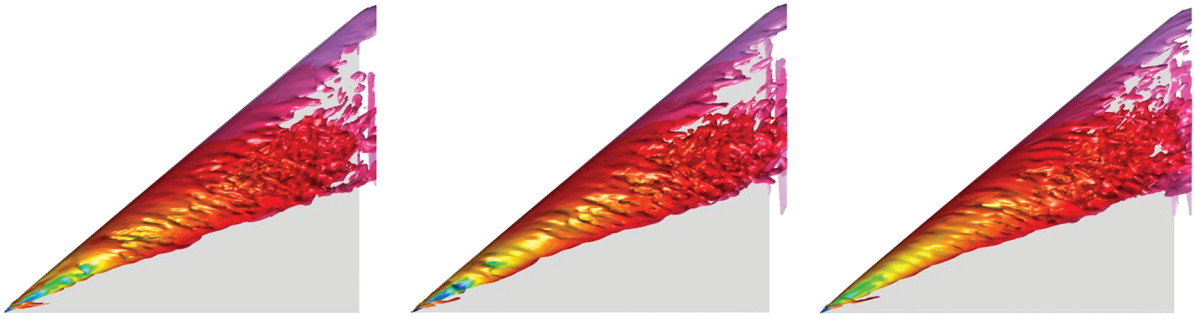

Fig. 18 Isosurfaces of constant axial vorticity colored by pressure: a) $Re = 2 \times 10^5$, b) $Re = 6.2 \times 10^5$, and c) $Re = 2 \times 10^6$.

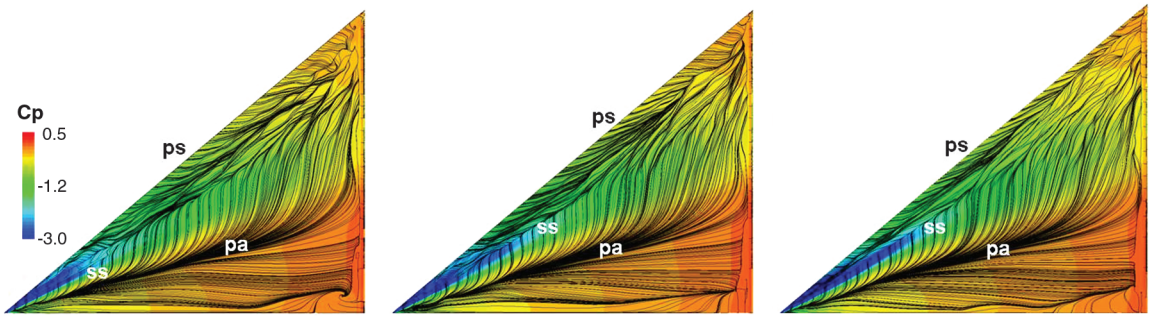

Fig. 19 Mean limiting streamline pattern showing the primary separation (ps), primary attachment (pa), secondary separation (ss), and surface pressure coefficient: a) $Re = 2 \times 10^5$, b) $Re = 6.2 \times 10^5$, and c) $Re = 2 \times 10^6$.

more numerous and distinct with increasing Reynolds number. At the lowest Reynolds number, Fig. 16a, an elongated secondary flow region exists. This secondary flow again reduces in size, and the secondary separation point moves outboard as the Reynolds number is increased.

Figure 17 displays the vortex structure on a plane downstream near the trailing edge, $\bar{x} = 0.875$. The peak levels of vorticity in the primary vortical flow region have weakened further and the separated vortical flow is composed of even finer-scale features. A clear secondary flow is only seen at the lowest Reynolds number. At the two higher Reynolds numbers, this secondary flow region becomes less and less distinct. As the Reynolds number is raised, the small-scale structures in the primary vortex do increasingly interact with the surface boundary layer at locations underneath the full span of the vortex (see, particularly, Fig. 17c). The thickening of the upper surface boundary layer near the symmetry plane is associated with the onset of transition in the surface boundary layer, which will be described more fully in Sec. VII.B.

The global structure of the mean small-scale features seen in the crossflow planes is more clearly represented by examining an isosurface of axial vorticity, Fig. 18. Two types of mean substructures can be observed in these figures. The first are helical substructures that corotate with the primary vortex. The development of these types of substructures in the mean flow has been described in a previous work by two of the present authors, Visbal and Gordnier [34], and is engendered by a complex transition process in the shear layer that rolls up to form the primary vortex. As the Reynolds number increases, these substructures decrease in wavelength and become more apparent. Their emergence is also observed progressively further upstream. The second feature seen in these figures are small-scale mean structures located in the core of the broken-down vortex.

C. Mean Surface Flow Features

An examination of the mean near-surface flowfield provides additional insight into the low-sweep delta wing flow and the impact of Reynolds number. The mean limiting streamline pattern for each Reynolds number is shown in Figs. 19a–19c. Primary separation occurs at the leading edge of the wing, with the primary attachment line located outboard of the symmetry plane. In between the primary attachment line and the leading edge, secondary separation occurs, with the secondary separation line moving outboard with increasing Reynolds number. The complexity of the surface streamline pattern in the outboard region of the delta wing magnifies as the trailing edge is approached. These complicated streamline patterns progress further upstream and inboard as the Reynolds number is increased. A region of separated flow is also observed inboard of the primary attachment line. The initiation of this separated flow region moves upstream as the Reynolds number is increased. This feature is associated with the onset of transition in the attached boundary layer near the symmetry plane.

Contours of the mean surface pressure coefficient are also plotted in Fig. 19. The low-pressure region outboard of the primary attachment line associated with the primary vortex is clearly visible. As the Reynolds number increases to 2×10^6, this region narrows and extends further downstream.

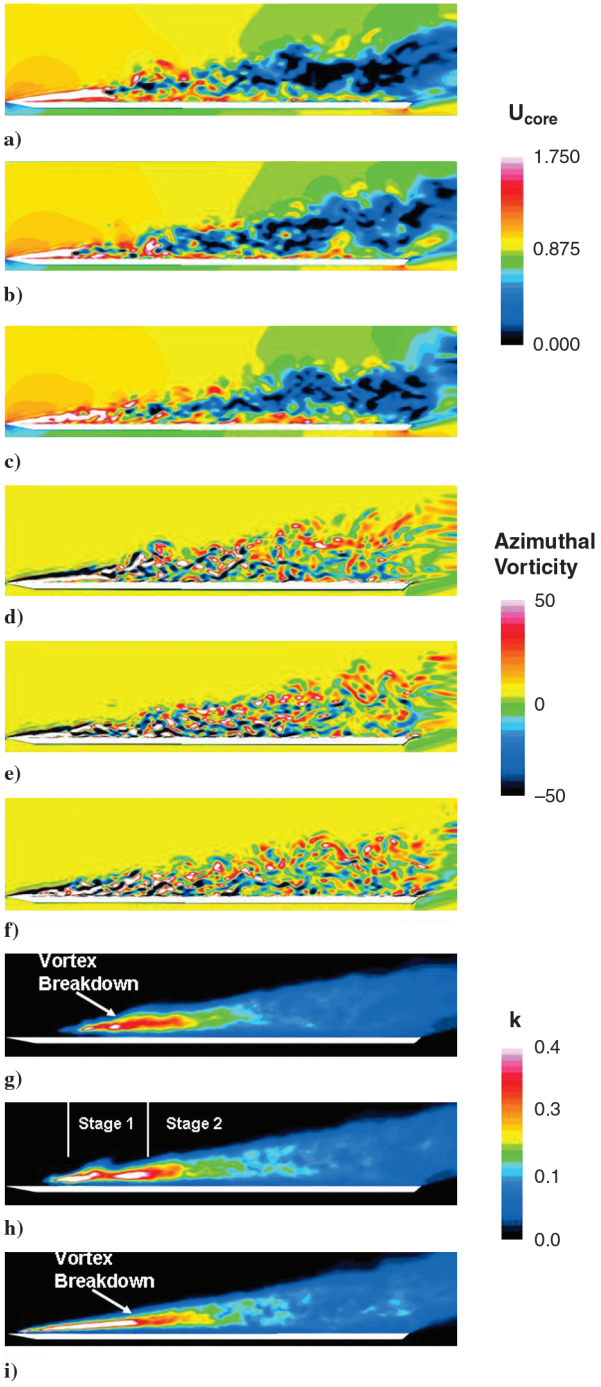

Fig. 20 Instantaneous axial velocity (a–c), azimuthal vorticity (d–f), and turbulent kinetic energy (g–i) on a plane through the vortex core: a, d, and g) $Re = 2 \times 10^5$; b, e, and h) $Re = 6.2 \times 10^5$; and c, f, and i) $Re = 2 \times 10^6$.

VII. Computed Instantaneous Flow Structure

A. Instantaneous Vortex Breakdown Structure

Figure 20 provides representations of the instantaneous vortex breakdown structure on a vertical plane through the vortex core. As in the mean flow, the characteristic jetlike flow in the vortex core is observed upstream of breakdown, Figs. 20a–20c. Downstream of breakdown, smaller-scale structures emerge as well as a predominantly wakelike flow. Small isolated regions of reversed axial flow (black regions in Figs. 20a–20c) are obtained at all Reynolds numbers. These regions become smaller as the Reynolds number increases. The dual-stage transformation of the vortex noted in the mean flow for $Re = 6.2 \times 10^5$, Fig. 13b, can also be discerned in Fig. 20b. The first stage of the transformation is characterized by a narrower region with pockets of both jetlike and wakelike flow. At the onset of the second stage, there is a thickening of the breakdown region and a more dominant wakelike flow is present. At the highest Reynolds number, Fig. 20c, undulations of the vortex core are noted resulting from the increasingly unsteady flow present upstream of breakdown.

Figures 20d–20f plot contours of azimuthal vorticity and highlight the disintegration of the coherent vortex core upstream of breakdown into fine-scale unsteady structures downstream. The switch in sign of azimuthal vorticity that characterizes the onset of vortex breakdown can be easily discerned for the two lower Reynolds numbers. The dual-stage nature of the vortex breakdown for $Re = 6.2 \times 10^5$ is again seen in Fig. 20e with a narrower region of small-scale structures after the initial switch in sign of azimuthal vorticity, followed by

thickening of the breakdown region at the onset of the second region. For $Re = 2 \times 10^6$, small-scale features are observed in the vortex core even ahead of breakdown, indicating increasing unsteadiness upstream of breakdown. The presence of these small-scale features makes it somewhat more difficult to clearly discern the switch in sign of azimuthal vorticity.

The highly unsteady nature of the flow is further revealed in Figs. 20g–20i, in which contours of the turbulent kinetic energy are displayed. At all Reynolds numbers, the highest levels of turbulent kinetic energy occur upstream of breakdown in the vortex core. At the highest Reynolds number, Fig. 20i, this region extends almost all the way to the apex. For $Re = 6.2 \times 10^5$, the high levels of turbulent intensity persist through the first stage of the breakdown of the vortex. At all three Reynolds numbers there is an area of moderate unsteadiness that starts at the onset of breakdown (stage 2 for $Re = 6.2 \times 10^5$) and extends downstream into the breakdown region. The values of turbulent kinetic energy decrease further as the trailing edge is approached.

The highly unsteady behavior upstream of breakdown can be better understood by examining the flow in a crossflow plane normal to the vortex core, Fig. 21. At locations upstream of breakdown there is a strong interaction of the leading-edge vortex with the surface boundary-layer flow that results in an eruptive response of the secondary flow with vorticity of the opposite sign being ejected from the surface and wrapped into the primary vortex (see, in particular, Fig. 21b). Accompanying this unsteady behavior is the development of small-scale vortices in the shear layer that rolls up to form the primary vortex. This highly unsteady interaction of the primary vortex with the surface boundary layer and the corresponding development of shear-layer instabilities has been described in detail by two of the present authors, Gordnier and Visbal, in [15,28–30,34]. This unsteady behavior leads to significant wandering of the vortex core, resulting in the high values of turbulent kinetic energy in the vortex core. The strongest interaction is observed for $Re = 6.2 \times 10^5$, Fig. 21e, with a weakening for the higher Reynolds number, $Re = 2 \times 10^6$, Fig. 21f. Higher levels of turbulent kinetic energy are also obtained in the secondary flow region, in which the secondary flow eruption process occurs, Fig. 21e.

Downstream of the breakdown point at $\bar{x} = 0.612$, Fig. 22, a clear vortex core is no longer discernible and there exists only a large region of unsteady small-scale structures. Also, no distinct secondary flow region exists, though pockets of vorticity of the opposite sign can be seen throughout the vortical flow region. The unsteady flow at this location results in a broad area of turbulent kinetic energy that covers the whole vortical flow region. The levels of turbulent kinetic energy show only a modest increase with Reynolds number and are substantially smaller than the peak values in the vortex core upstream of breakdown. Further downstream, at $\bar{x} = 0.875$, the flow has broken down into even finer structures, Fig. 23. A corresponding further reduction of the turbulent kinetic energy levels is seen, Figs. 23d–23f.

B. Transitional Flow Region Near the Symmetry Plane

In Fig. 19, a separated flow region was noted inboard of the primary attachment toward the symmetry plane. This mean separated flow region is associated with the onset of transition in the surface boundary layer near the symmetry plane and may be further understood by examining contours of the spanwise component of vorticity on the midplane, Figs. 24a–24c, and on the surface, Figs. 24d–24f.

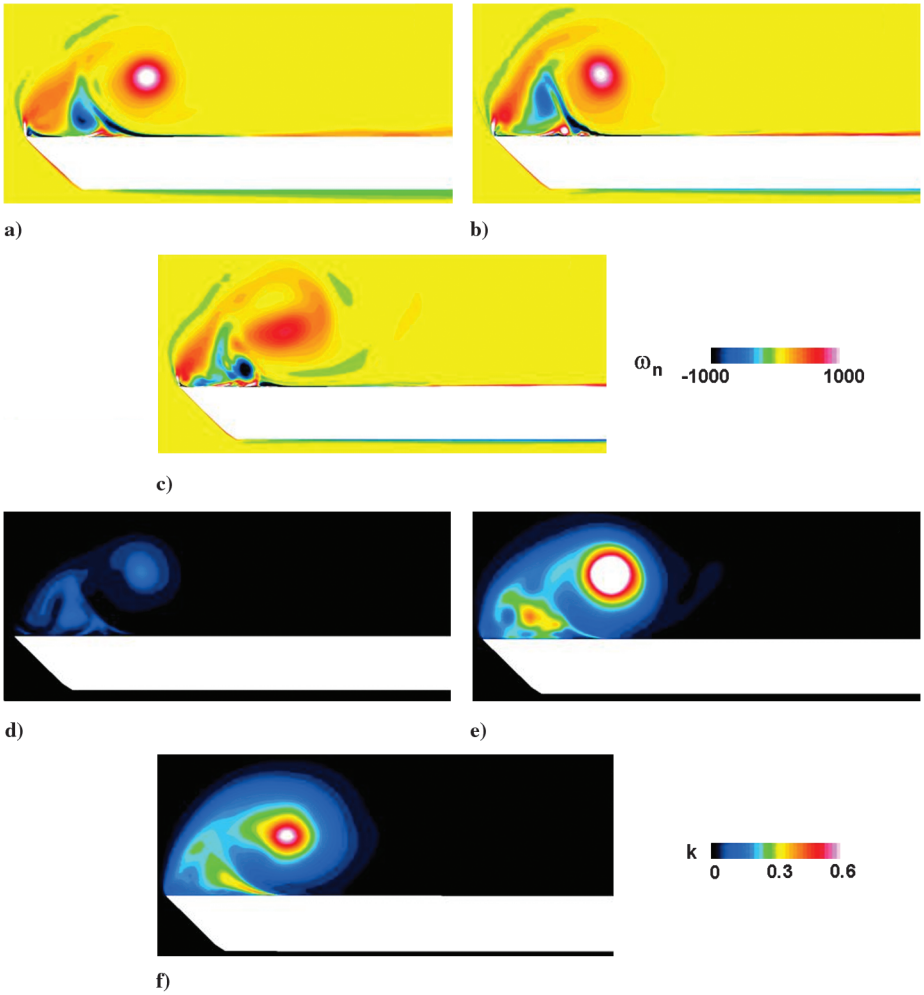

Fig. 21 Instantaneous axial vorticity (a–c) and turbulent kinetic energy (d–f) on a crossflow plane normal to the vortex core $\bar{x} = 0.175$: a, d) $Re = 2 \times 10^5$; b, e) $Re = 6.2 \times 10^5$; and c, f) $Re = 2 \times 10^6$.

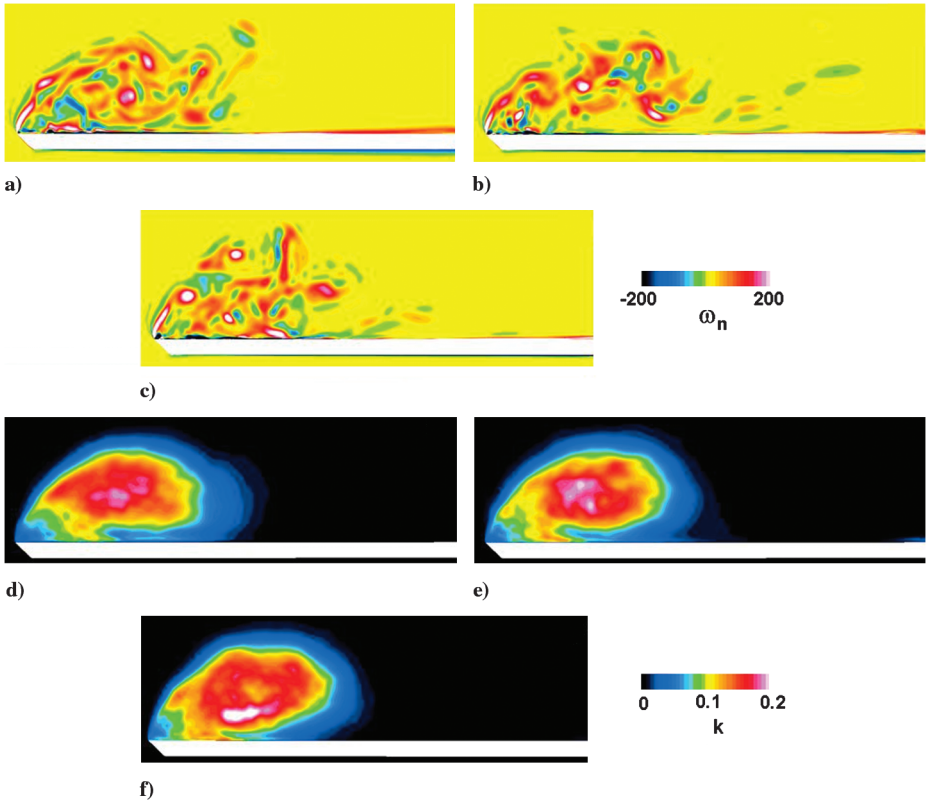

Fig. 22 Instantaneous axial vorticity (a–c) and turbulent kinetic energy (d–f) on a crossflow plane normal to the vortex core, $\bar{x} = 0.612$: a, d) $Re = 2 \times 10^5$; b, e) $Re = 6.2 \times 10^5$; and c, f) $Re = 2 \times 10^6$.

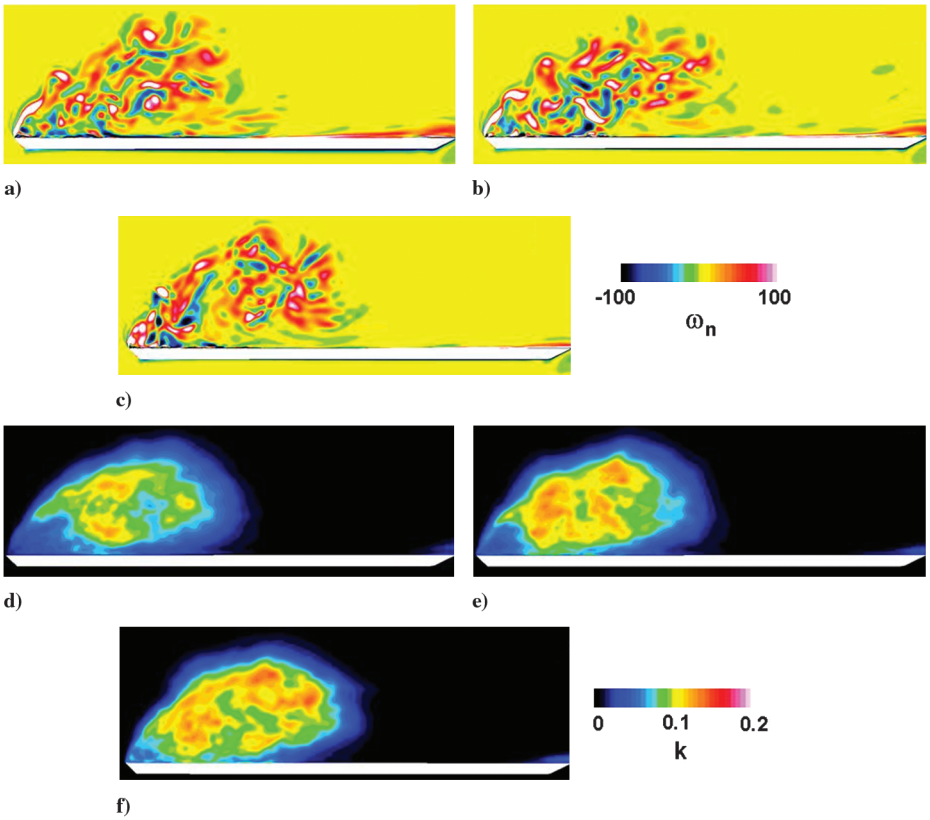

Fig. 23 Instantaneous axial vorticity (a–c) and turbulent kinetic energy (d–f) on a crossflow plane normal to the vortex core $\bar{x} = 0.875$: a, d) $Re = 2 \times 10^5$; b, e) $Re = 6.2 \times 10^5$; and c, f) $Re = 2 \times 10^6$.

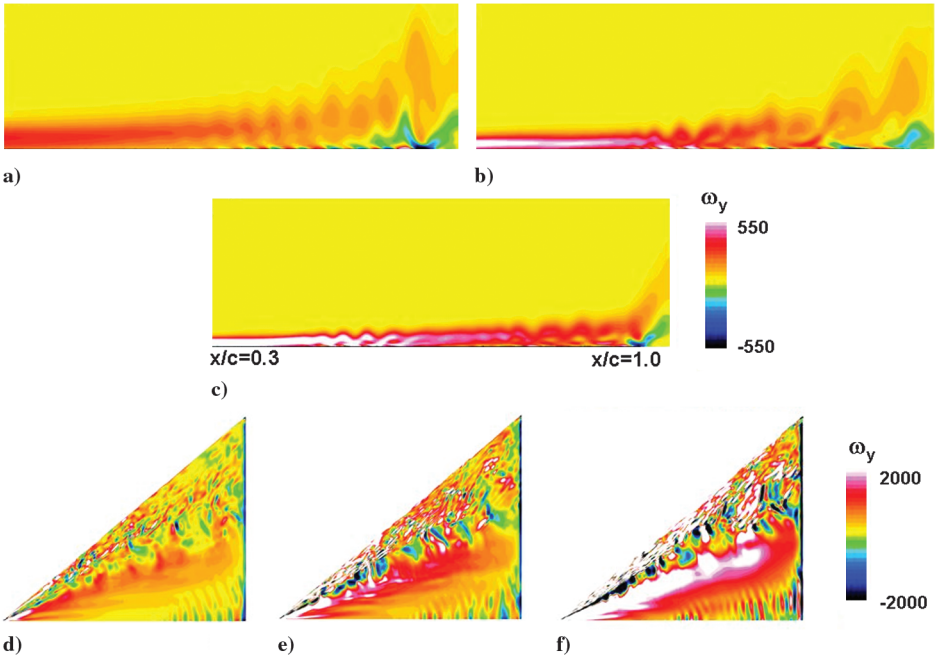

Fig. 24 Instantaneous spanwise vorticity on the symmetry plane (a–c) and on the wing surface (d–f): a, d) $Re = 2 \times 10^5$; b, e) $Re = 6.2 \times 10^5$; and c, f) $Re = 2 \times 10^6$.

The onset of an instability layer and the subsequent roll up and separation of the boundary layer is portrayed in Figs. 24a–24c. Note that these figures have been magnified in the z direction by a factor of 10. This unsteady boundary-layer flow is characterized by the formation of small-scale vortical structures that are subsequently convected downstream. These vortices interact with the surface, creating small regions of vorticity of the opposite sign near the surface. As the Reynolds number is increased, Figs. 24a–24c, the boundary layer thins and the onset of the instability moves progressively upstream. Both the upstream and spanwise extent of this transitional flow region can be more plainly seen in Figs. 24d–24f, in which the imprint of the transitional boundary layer is seen as fingerlike structures extending outboard from the symmetry plane and terminating inboard of the primary attachment line. The growth of the instability region with increasing Reynolds number is again apparent in these figures.

It is quite likely that further grid resolution is required near the symmetry plane to fully capture this transitional/turbulent flow. The impact of the symmetry boundary condition also needs to be further explored. Nonetheless these computations highlight the very complex surface boundary-layer flows that may develop for this type of low-sweep delta wing geometry at these moderate Reynolds numbers. High-fidelity techniques such as the ILES approach presented here will be needed to accurately capture these complex, mixed-type flows.

VIII. Conclusions

Computations have been performed for a 50-deg-sweep delta wing at a 15 deg angle of attack and moderate Reynolds numbers of $Re = 2 \times 10^5$, 6.2×10^5, and 2×10^6. A sixth-order compact-difference scheme coupled with an eighth-order low-pass filter has been used to solve the Navier–Stokes equations. An implicit LES scheme exploits the use of the low-pass filters to regularize the solution for these transitional Reynolds numbers. An assessment of grid resolution showed that significant smaller scales are captured on the finer mesh, providing a more accurate representation of the complex, unsteady, separated flow. These results highlight the importance of both high-order accuracy and grid resolution in correctly simulating these types of transitional flows.

Particle image velocimetry measurements were made for the 50-deg-sweep delta wing for the two lower Reynolds numbers computed, $Re = 2 \times 10^5$ and 6.2×10^5. At the lower Reynolds number, good agreement was seen between the computation and the experiment, with all the salient features of the experiment being reproduced for both the mean and instantaneous flowfields. Good qualitative agreement is again seen for the higher Reynolds number, $Re = 6.2 \times 10^5$, with some differences in the location and structure of the onset of vortex breakdown. The overall good agreement between the computation and experiment provides confidence in the ability of the ILES approach to simulate these moderate Reynolds number flows.

A detailed description of the computed mean and instantaneous flow structure over the delta wing has been given, including a discussion of the effect of Reynolds number on the unsteady flowfield. The vortex breakdown location was observed to initially move upstream and then subsequently downstream with increasing Reynolds number. For $Re = 6.2 \times 10^5$, the breakdown appears to occur in two stages, with a diffuse region of lower axial velocities followed by a region of stronger wakelike flow. The highest levels of turbulent kinetic energy are observed upstream of breakdown and in the first region of the breakdown for $Re = 6.2 \times 10^5$. This leads to increased turbulent dissipation and a weakening of the intact vortical flow upstream of breakdown with increasing Reynolds number. In crossflow planes normal to the vortex core, a weakening of the secondary flow and an outboard movement of the secondary separation point were observed, with increasing Reynolds number both upstream and downstream of breakdown. Downstream of breakdown, the vortex takes a more oval shape and is composed of a number of small-scale features that become more numerous and distinct with increasing Reynolds number. The mean flow exhibits helical substructures that corotate with the primary vortex in the shear layer that separates from the leading edge and rolls up to form the primary vortex. These substructures decrease in wavelength and develop progressively further upstream with increasing Reynolds number.

Transition of the surface boundary layer near the symmetry plane was also noted. This unsteady boundary layer flow is characterized by the formation of small-scale vortical structures and their subsequent convection downstream. The onset of the instability in the boundary layer moves progressively upstream with increasing Reynolds number. Although it is likely that further computations are required to fully understand this transitional/turbulent flow, the

presence of this transitional flow region highlights why high-fidelity techniques such as the present ILES approach are needed to model the complex mixed-type flows existing at moderate Reynolds numbers.

Acknowledgments

The computational portion of this work was sponsored by the U.S. Air Force Office of Scientific Research under a task monitored by Rhett Jefferies and supported in part by a grant of high-performance computer (HPC) time from the U.S. Department of Defense HPC Shared Resource Centers at the Naval Oceanographic Office and the Aeronautical Systems Center. The experimental work was sponsored by the U.S. Air Force Office of Scientific Research, U.S. Air Force Materiel Command, U.S. Air Force under grant number FA8655-06-1-3058 and also by an Engineering and Physical Sciences Research Council Academic Fellowship in Unmanned Air Vehicles.

References

[1] Morton, S. A., Forsythe, J., Mitchell, A., and Hajek, D., "DES and RANS Simulations of Delta Wing Vortical Flows," AIAA Paper 2002-0587, Jan. 2002.

[2] Morton, S. A., "High Reynolds Number DES Simulations of Vortex Breakdown over a 70 m Degree Delta Wing," AIAA Paper 2003-4217, June 2003.

[3] Görtz, S., "Detached-Eddy Simulations of a Full-Span Delta Wing at High Incidence," AIAA Paper 2003-4216, June 2003.

[4] Gaitonde, D., and Visbal, M., "High-Order Schemes for Navier–Stokes Equations: Algorithm and Implementation into FDL3DI," Air Force Research Laboratory Tech. Rep. TR-1998-3060, Wright–Patterson Air Force Base, OH, 1998.

[5] Gaitonde, D., and Visbal, M., "Further Development of a Navier–Stokes Solution Procedure Based on Higher-Order Formulas," AIAA Paper 99-0557, Jan. 1999.

[6] Visbal, M., and Gaitonde, D., "High-Order Accurate Methods for Complex Unsteady Subsonic Flows," *AIAA Journal*, Vol. 37, No. 10, 1999, pp. 1231–1239. doi:10.2514/2.591

[7] Visbal, M. R., and Gaitonde, D. V., "On the Use of Higher-Order Finite-Difference Schemes on Curvilinear and Deforming Meshes," *Journal of Computational Physics*, Vol. 181, 2002, pp. 155–185. doi:10.1006/jcph.2002.7117

[8] Sherer, S., and Visbal, M. R., "Computational Study of Acoustic Scattering from Multiple Bodies Using a High-Order Overset Grid Approach," AIAA Paper 2003-3203, 2003.

[9] Sherer, S. E., and Scott, J. N., "High-Order Compact Finite-Difference Methods on General Overset Grids," *Journal of Computational Physics*, Vol. 210, 2005, pp. 459–496. doi:10.1016/j.jcp.2005.04.017

[10] Visbal, M. R., Morgan, P. E., and Rizzetta, D. P., "An Implicit LES Approach Based on High-Order Compact Differencing and Filtering Schemes (Invited)," AIAA Paper 2003-4098, June 2003.

[11] Ol, M. V., and Gharib, M., "Leading-Edge Vortex Structure of Nonslender Delta Wings at Low Reynolds Number," *AIAA Journal*, Vol. 41, No. 1, 2003, pp. 16–26. doi:10.2514/2.1930

[12] Taylor, G. S., Schnorbus, T., and Gursul, I., "An Investigation of Vortex Flows over Low Sweep Delta Wings," AIAA Paper 2003-4021, June 2003.

[13] Taylor, G., and Gursul, I., "Buffeting Flows over a Low Sweep Delta Wing," *AIAA Journal* Vol. 42, No. 9, 2004, pp. 1737–1745. doi:10.2514/1.5391

[14] Yaniktepe, B., and Rockwell, D., "Flow Structure on a Delta Wing of Low Sweep Angle," *AIAA Journal*, Vol. 42, No. 3, 2004, pp. 513–523. doi:10.2514/1.1207

[15] Gordnier, R. E., and Visbal, M. R., "Compact Difference Scheme Applied to Simulation of Low-Sweep Delta Wing Flow," *AIAA Journal*, Vol. 43, No. 8, 2005, pp. 1744–1752. doi:10.2514/1.5403

[16] Gursul, I., "Review of Unsteady Vortex Flows over Slender Delta Wings," *Journal of Aircraft*, Vol. 42, No. 2, 2005, pp. 299–319. doi:10.2514/1.5269

[17] Gursul, I., Gordnier, R. E., and Visbal, M., "Unsteady Aerodynamics of Nonslender Delta Wings," *Progress in Aerospace Sciences*, Vol. 41, No. 7, 2005, pp. 515–557. doi:10.1016/j.paerosci.2005.09.002

[18] Gordnier, R. E., and Visbal, M. R., "High-Order Simulation of Low Sweep Delta Wing Flows Using ILES and Hybrid RANS/ILES Models," AIAA Paper 2006-504, Jan. 2006.

[19] Anderson, D., Tannehill, J., and Pletcher, R., *Computational Fluid Mechanics and Heat Transfer*, McGraw–Hill, New York, 1984.

[20] Lele, S., "Compact Finite Difference Schemes with Spectral-Like Resolution," *Journal of Computational Physics*, Vol. 103, 1992, pp. 16–42. doi:10.1016/0021-9991(92)90324-R

[21] Gaitonde, D., Shang, J., and Young, J., "Practical Aspects of High-Order Accurate Finite-Volume Schemes for Electromagnetics," AIAA Paper 97-0363, Jan. 1997.

[22] Alpert, P., "Implicit Filtering in Conjunction with Explicit Filtering," *Journal of Computational Physics*, Vol. 44, 1981, pp. 212–219. doi:10.1016/0021-9991(81)90047-4

[23] Beam, R., and Warming, R., "An Implicit Factored Scheme for the Compressible Navier–Stokes Equations," *AIAA Journal*, Vol. 16, No. 4, 1978, pp. 393–402. doi:10.2514/3.60901

[24] Jameson, A., Schmidt, W., and Turkel, E., "Numerical Solutions of the Euler Equations by a Finite Volume Method Using Runge–Kutta Time Stepping Schemes," AIAA Paper 81-1259, 1981.

[25] Pulliam, T., "Artificial Dissipation Models for the Euler Equations," *AIAA Journal*, Vol. 24, No. 12, 1986, pp. 1931–1940. doi:10.2514/3.9550

[26] Pulliam, T., and Chaussee, D., "A Diagonal Form of an Implicit Approximate-Factorization Algorithm," *Journal of Computational Physics*, Vol. 39, No. 2, 1981, pp. 347–363. doi:10.1016/0021-9991(81)90156-X

[27] Visbal, M., and Gaitonde, D., "Very High-Order Spatially Implicit Schemes for Computational Acoustics on Curvilinear Meshes," *Journal of Computational Acoustics*, Vol. 9, No. 4, 2001, pp. 1259–1286. doi:10.1142/S0218396X01000541

[28] Gordnier, R. E., and Visbal, M. R., "Unsteady Vortex Structure over a Delta Wing," *Journal of Aircraft*, Vol. 31, No. 1, Jan.–Feb. 1994, pp. 243–248. doi:10.2514/3.46480

[29] Visbal, M. R., and Gordnier, R. E., "Origin of Computed Unsteadiness in the Shear Layer of Delta Wings," *Journal of Aircraft*, Vol. 32, No. 5, 1995, pp. 1146–1148. doi:10.2514/3.46850

[30] Gordnier, R. E., and Visbal, M. R., "Instabilities in the Shear Layer of Delta Wings," AIAA Paper 95-2281, June 1995.

[31] Rockwell, D., "Three-Dimensional Flow Structure on Delta Wings at High Angle of Attack: Experimental Concepts and Issues," AIAA Paper 93-0550, Jan. 1993.

[32] Visbal, M. R., "Computed Unsteady Structure of Spiral Vortex Breakdown on Delta Wings," AIAA Paper 96-2074, June 1996.

[33] Brown, G., and Lopez, J., "Axisymmetric Vortex Breakdown, Part 2. Physical Mechanisms," *Journal of Fluid Mechanics*, Vol. 221, 1990, pp. 553–576. doi:10.1017/S0022112090003676

[34] Visbal, M. R., and Gordnier, R. E., "On the Structure of the Shear Layer Emanating form a Swept Leading Edge at Angle of Attack," AIAA Paper 2003-4016, June 2003.

J. Sahu
Associate Editor